Microstructural Evaluation and Corrosion Resistance of Semisolid Cast A356 Alloy Processed by Equal Channel Angular Pressing

Mohamed Abdelgawad Gebril [1,2], Mohd Zaidi Omar [1,*] , Intan Fadhlina Mohamed [1,3] and Norinsan Kamil Othman [4]

[1] Centre for Materials Engineering and Smart Manufacturing, Universiti Kebangsaan Malaysia, 43600 UKM Bangi, Malaysia; gebril.ukm@gmail.com (M.A.G.); intanfadhlina@ukm.edu.my (I.F.M.)
[2] Department of Mechanical Engineering, Faculty of Engineering, Benghazi University, 16063 Benghazi, Libya
[3] Fuel Cell Institute, Universiti Kebangsaan Malaysia, 43600 UKM Bangi, Malaysia
[4] Department of Applied Physics, Faculty of Science and Technology, Universiti Kebangsaan Malaysia, 43600 UKM Bangi, Malaysia; insan@ukm.edu.my
* Correspondence: zaidiomar@ukm.edu.my; Tel.: +603-8921-4831

Abstract: As-cast and semisolid casting using a cooling slope A356 alloy were processed by equal channel angular pressing (ECAP) for Si and grain refinement. The ECAP was conducted at room temperature in a mold, with a channel angle of 120°, and this resulted in a significant size reduction of grain and Si particles from 170.5 and 4.22 to 23.12 and 0.71 μm, respectively, after six passes of heat-treated cooling slope casting, using the ECAP process. The hardness increased with ECAP processing, from 61 HV, for the as-cast alloy, to 134 Hv, after six passes of heat-treated cooling slope casting. The corrosion resistance of the alloy improved, from 0.042 to 0.0012 mmy^{-1}, after the ECAP process. In this work both the strength and corrosion resistance of the ECAPed A356 alloys were improved with the application of the cooling slope process than without (i.e., from the as-cast condition).

Keywords: A356 alloy; cooling slope; ECAP; hardness; pitting corrosion

1. Introduction

A356 alloy is an Al–Si casting alloy that contains ~7 wt.% Si, mostly developed for automotive powertrain components such as the engine block and automotive transmission cases. However, the solubility limitation of silicon (Si) in aluminum (Al) contributes to the precipitation of flake-shaped Si particles with sharp edges, which significantly affects the mechanical and electrochemical properties.

The coarse flake Si particles can cause the initiation of premature cracks during deformation. Consequently, this shape weakens the workability of the alloy at room temperature, thus reducing the ductility of the alloy [1]. The morphology of Si particles and its distribution play essential roles in the electrochemical properties of Al–Si alloy. The cathodic behavior of Si within the Al-rich matrix contributes to the occurrence of localized corrosion, with the formation of microgalvanic couples [2,3], which also leads to poor mechanical behavior, such as in stent applications [4]. The reduction in the area ratio of noble Si particles (cathode) to less-noble eutectic Al phase (anode) around Si particles largely improves pitting corrosion resistance. In other words, the reduction in the area ratio of cathode to anode (Ac/Aa) reduces the corrosion current density. In the Al–Si alloy, the size reduction of Si particles which as cathode, facilitates the re-passivation of protective film with improved stability [5–7].

Since the corrosion resistance and strength of alloys are mostly influenced by their microstructure [8–10], there are various methods to refine the microstructure of unmodified A356 alloy

in order to improve the corrosion resistance and mechanical properties, such as heat treatment [11–13] and semisolid state processing to obtain a spherical microstructure using mechanical stirring, electromagnetic stirring, and controlled nucleation methods [14–16]. The cooling slope casting process is also considered as another simple method of the semisolid metal casting process to produce feedstock material, with a spheroid microstructure, which bears minimal equipment and operational costs [17–19]. The severe plastic deformation (SPD) technique effectively accommodates the combination of major grain refinement and Hall-Petch strengthening in bulk billets, where the working piece is subjected to extensive strains of cold or warm processing. Fundamentally, the SPD technique is eminently capable of effectively refining the structure of grain down to an ultrafine micrometer-scale or nano-scale due to the agglomeration of dislocation, which leads to the formation of subgrains. In particular, this technique enables various metals and metallic alloys that are brittle and ductile to achieve the structure of refined grain [20–22].

The equal channel angular pressing (ECAP) of SPD the technique is considered the most effective technique in fabricating bulk ultrafine-grained materials [23]. Some researchers have applied several methods of SPD to Al–Si alloy to improve the corrosion resistance of the alloy through microstructural refinement. In one study, [24,25] it was concluded that the improvement of the corrosion resistance and mechanical properties of pure aluminum and A356 alloy was due to microstructure refinement. In another study, the effect of ECAP processing on the corrosion resistance of Al—11wt.% Si [26], it was reported that the great refinement of both the matrix microstructure and the Si particles after severe plastic deformation leads to an improvement of the corrosion resistance.

In another research [27] on the Anticorrosion behavior of ultrafine-grained Al—26 wt.% Si alloy fabricated by ECAP, it was reported that the improvement of ECAPed Al—26 wt.% Si alloy corrosion resistance results from the homogeneous ultrafine structure, with the breakage of brittle large primary silicon crystals. SPD processing improves the corrosion resistance and mechanical properties of Al–Si alloy [28].

However, the reduction of both grain size and eutectic Si particles through the deformation process may alter the corrosion property of the alloy [10,29,30]. Addressing these issues, the present study aimed to refine Si particles and to produce material with a uniform microstructure through the combination of the cooling slope casting process and ECAP processing at room temperature. The effect of T6 heat treatment was studied to determine the microstructure changes after ECAP processing. This study further examined the effects of microstructure changes and its effect on strength as well as corrosion resistance for both ECAPed as-cast and ECAPed cooling slope-cast A356 alloy.

2. Materials and Methods

This study used cast commercial A356 (Si—7 wt.%, Mg—0.149 wt.%, Fe—0.126 wt.%, Cu—0.01 wt.%, Mn—0.002 wt.%, Zn—0.006 wt.%, Cr—0.001 wt.%, Ti—0.178 wt.%) alloy casted in ingot, with initial dimensions of 80 mm $\times$ 40 mm $\times$ 140 mm (width $\times$ thickness $\times$ length). Using a graphite crucible, the as-cast was melted at a temperature of 750 °C. For the cooling slope casting process, the cooling slope of stainless steel, with a slope length of 250 mm as well as a tilt angle of 60°, was used. The reason for selecting these conditions was based on our work [31]. The apparatus used for this process is shown in Figure 1a. This study specifically selected 620 °C as the pouring temperature to limit the superheating of the melt [31]. The molten metal was poured downward, on a stainless steel slope, into a mold with a vertical surface, before quenching in water. In line with the T6 procedure, this study performed a heat treatment process to the as-cast and cooling slope-cast samples, which involved the following processes in this order: (1) an eight-hour sequence of solution treatment at 540 °C, (2) water quenching, and (3) three-hour aging process at a temperature of 180 °C [32]. Following that, as illustrated in Figure 1b, as-cast and cooling slope-cast samples were machined into a rod shape, with a diameter of 9.8 mm. The samples were ECAPed in a die with a channel angle of 120°, following route A (where the sample is not rotated between each pass). It should be noted that molybdenum disulfide (MoS_2) grease was used as a lubricant in this study.

The pressing of as-cast and cooling slope-cast A356 alloy samples was carried out using a 50-ton hydraulic press. As-cast samples were pressed up to four passes, without any cracks on the surface while the cooling slope casting samples were successfully pressed to six passes.
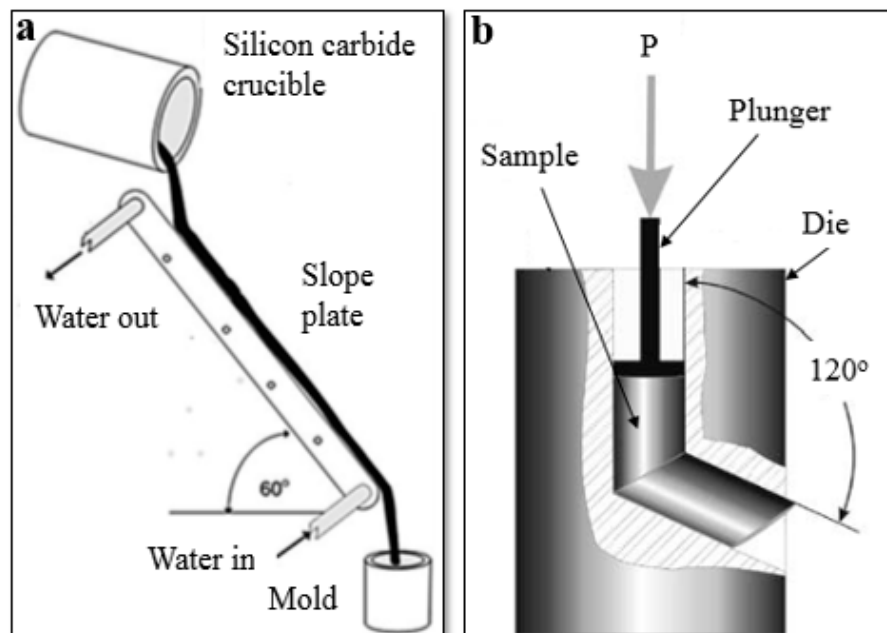
Figure 1. Schematic of (**a**) cooling slope casting and (**b**) ECAP mold.

Both ECAPed samples were subsequently examined under a field emission scanning electron microscope (FESEM, Zeiss, Oberkochen, Germany) and optical microscope (OM, Olympus corporation, Tokyo, Japan). Additionally, an energy dispersive x-ray (EDX) (equipped to FESEM) was used for elemental analysis. A Vickers hardness tester (micro Vickers hardness tester, Zwick, Germany; ZHVμ) was used to measure the hardness of the average of three samples per case. These samples were also prepared for microstructure analysis using silicon carbide (SiC) papers of grit between 180 and 2000, followed by a polishing process using 3 μm and 1 μm of diamond paste (Al_2O_3). Meanwhile, an etching process was performed using Keller's reagent (1% HF, 1.5% HCl, 2.5% HNO_3, H_2O solution) as an etchant. This study performed quantitative metallography analysis to measure the grain size, according to the ASTM E112 standard. The size of Si particles (the width and length of particles) was measured using the Smart Tiffv2 software, considering at least 200 particles in each case. Following that, an electrochemical experiment was performed in naturally aerated 3.5% NaCl solution at room temperature, with pH 6.5. A potentiostat GAMRY 3.2 was used to measure the rate of corrosion (characterized by i_{corr}) of these samples. For this, a three-electrode cell was used, which comprised of (1) test material (as a working electrode), (2) graphite (as a counter electrode), and (3) a silver or silver chloride (Ag or AgCl) electrode (as a reference electrode). The potential dynamic polarization tests were performed at a scanning rate of 1 mV s^{-1} with a range from -250 mV versus open circuit potential (OCP) to the final potential of 250 mV versus OCP. The potentiodynamic tests were started after about 15 min of immersion in 3.5% NaCl. Immersion tests were performed during 14 days in 3.5 wt.% NaCl naturally aerated solution to study the surface appearance. Basically, each sample was mounted in epoxy that was aired for 24 hours. Finally, these samples were smoothened using up to 1200-grit SiC before each corrosion test.

3. Results and Discussion

3.1. The Effect of Cooling Slope

Figure 2 shows the microstructure of the as-cast A356 alloy sample, before and after the cooling slope casting process. Typically, the primary α-Al phase (bright phase), which is surrounded by eutectic phase (dark phase), is formed during the initial solidification phase.
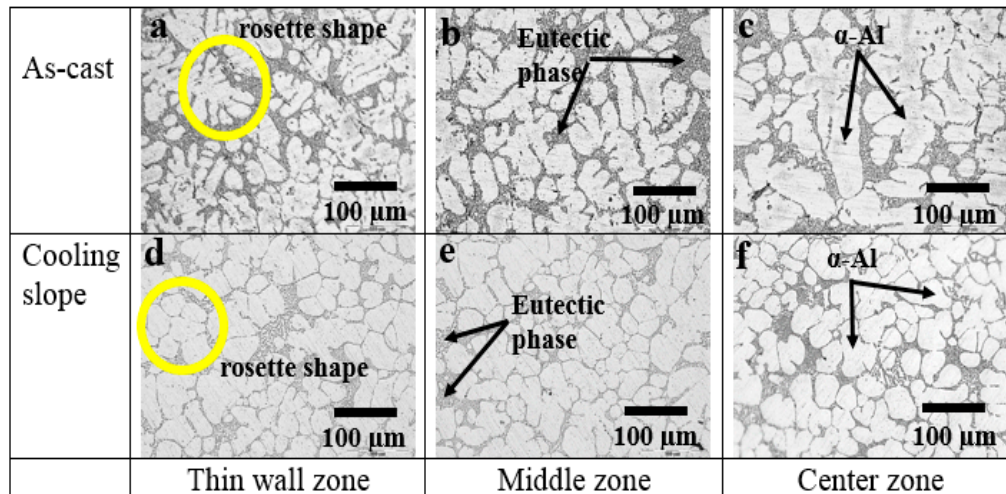
Figure 2. Microstructure of as-cast (**a**–**c**) and cooling slope casting samples (**d**–**f**). (**a**) coarse dendritic and rosette shape of α-Al phase at thin wall zone; (**b**) and (**c**) dendritic shape in the middle and center zone in as-cast samples; (**d**) rosette shape of α-Al phase at thin wall zone; (**e**) and (**f**) nearly globular shape at the middle and in the center zone of cooling slope samples.

The morphology of primary α-Al phase in three zones was found to be mostly dendritic for the as-cast sample, before the cooling slope casting process, as displayed in Figure 2a–c. However, the evolution of the coarsen dendritic to finer dendritic could be observed from the center zones approaching the thin wall zone. The variation in cooling rate depends on the location in the mold and affects the morphology of the primary α-Al phase. Considering that the mold itself has a relatively low initial temperature, the cooling rate is more rapid near the wall of the mold, thus leading to the nucleation of numerous grains of random orientations in the thin wall zone area [33]. During the pouring of molten alloy, the presence of forced convection detaches the dendritic arms that developed in the thin wall zone area. However, the dendrites start to form in the middle zone due to the lower cooling rates in this zone. They later grew and become ripened as coarse dendrites as a result of the lowest cooling rate in this center zone [34].

The non-dendritic microstructures of the as-cast A356 sample, after the cooling slope casting process, are shown in Figure 2d–f. However, in particular, the morphology of the primary α-Al phase in the thin wall zone appeared rosette-like Figure 2d and almost globular-like in the middle zone and center zone Figure 2e–f. In the center zone, the primary α-Al phase was found to be coarser than that in the middle zone. This may be because the temperature gradient across these three sections during solidification contributes to the variation in the morphology and size of the primary α-Al phase in these three zones. The slowest cooling rate in the center zone allows the α-Al phase to grow courser, as the cooling time is prolonged.

3.2. The Heat Treatment Solution

Alloy A356 is a heat-treatable hypoeutectic Al–Si alloy. Figure 3a–b shows optical micrographs of the both the primary α-Al phase and the eutectic Si particles in both alloy samples, before the heat treatment process. As for the primary α-Al phase (bright phase), grains with a globular structure could

be observed in the cooling slope-cast alloy sample, while large grain, surrounded by coarse eutectic constituents (dark phase), appeared in the as-cast alloy sample. The flake and acicular morphology of Si particles in as-cast and in cooling slope samples were transformed into a spheroidized shape after T6 heat treatment, as shown in Figure 3c–d. In a solution heat treatment sample, the eutectic Si particles were fragmented and spheroidized during the coarsening processes [35,36]. It was observed that the eutectic Si particles were refined and had fewer sharp angles edges, as in the as-cast alloy before heat treatment. The same behavior was reported by previous studies, which found that the T6 heat treatment process initiated the spheroidization of Si particles [37,38], but a considerable amount of acicular shapes remained after the T6 heat treatment process.
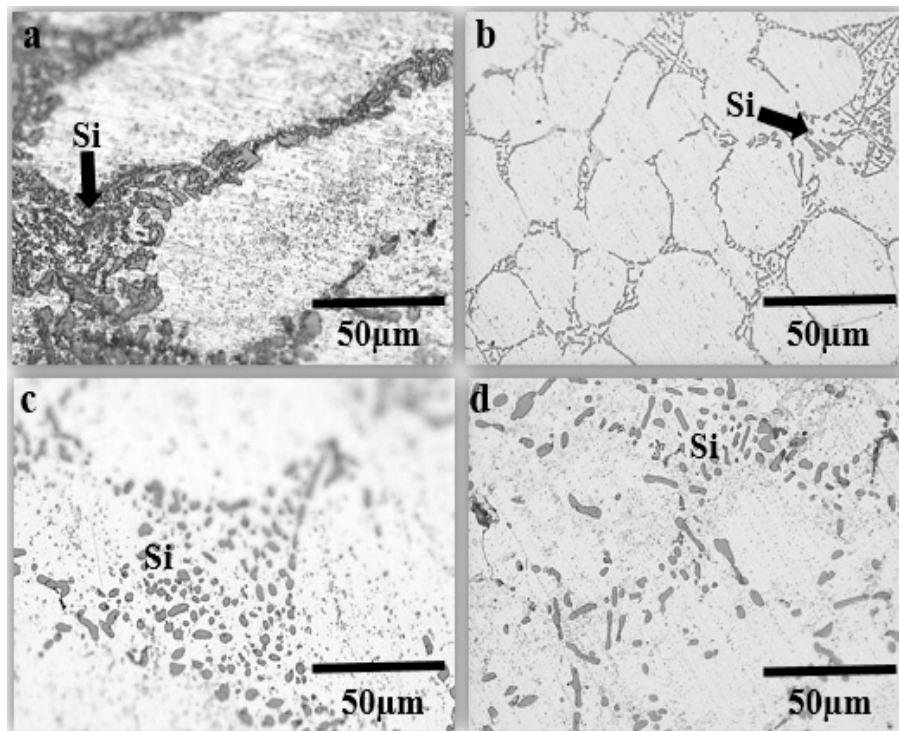
Figure 3. Microstructure of eutectic phase: (**a**) as-cast, (**b**) cooling slope, (**c**) as-cast-T6 and (**d**) cooling slope-T6.

3.3. Process of ECAP

The microstructures of the as-cast-T6 and cooling slope-cast-T6 alloy samples, subjected to four passes of route A, were displayed in Figure 4a–b. Meanwhile, following route A, the microstructure of cooling slope-cast-T6 alloy samples, which was subjected to six passes of ECAP, is shown in Figure 4c. The primary α-Al phase and eutectic constituents were elongated into plate-like shapes for the as-cast alloy sample [39], but fibrous-like shapes, for the latter samples. As shown in Table 1, the Si particles and eutectic phase appeared to be finer in both as-cast and cooling slope-cast alloy samples, after ECAP processing. Due to ECAP processing, the distribution was observed to be more uniform in the cooling slope-cast alloy sample. The result determined agrees with our earlier study, which reported that refine Si particles were observed through the cooling slope casting of alloy [40]. Nonetheless, the spheroidization and fragmentation of Si particles in this study were acquired through the T6 heat treatment process, coupled with the ECAP process.
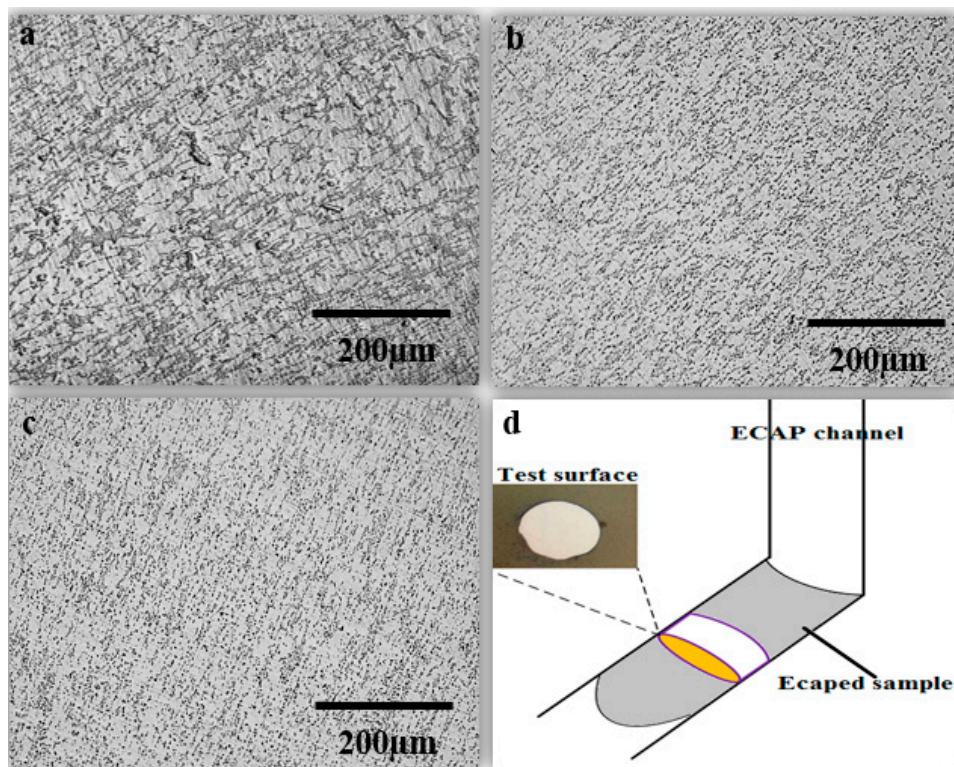
Figure 4. Microstructure of ECAPed-T6 A356 alloy (**a**) as-cast after 4 passes, (**b**) cooling slope after 4 passes, (**c**) cooling slope after 6 passes and (**d**) surface of microscopic ECAPed sample.

Based on the microstructures of both samples, following route A, the refining and the distribution of both primary the α-Al phase and eutectic constituents in the ECAPed cooling slope-cast sample became more homogeneous. Thus, the microstructure changes may lead to changes in the mechanical and electrochemical properties of the alloy [28,41–43]. This is due to the reduction and distribution of cathodic to anodic phases. The straining led to the formation of dislocated cell structures, with a high dislocation density. The dislocation remains within the cell structures, which do not affect the remaining cell boundaries or develop walls that separate these cells into smaller cells. However, persistent shear straining processes may lead to a saturated dislocation density within these cell structures, which could be significantly reduced through (i) enhanced dynamic recovery (which would stabilize the creation and annihilation of dislocations) and (ii) the conversion of cells to well-defined grains (which would cause severe movement of cell interior dislocations to cell boundaries). In fact, this suggested that the process of grain refinement depends on the level of straining or in other words, the generation of dislocations [44–46].

3.4. Scanning Electron Microscope (FESEM)

Table 1 shows the grain refinement and Si particles fragmentation after ECAP processing. Figure 5a–b shows the scanning electron microscope (SEM) micrographs of the ECAPed as-cast and cooling slope-cast samples. The Si particles appeared finer in the ECAPed cooling slope than in the ECAPed as-cast. With the continuous passes, the Si particles and eutectic mixture were broken down and fragmented into finer particles, as shown in Figure 5c–d.

Table 1. Average size of grain size and Si particles before and after ECAP.

Samples	Si Size (μm)	Grain Size (μm)
As-cast	4.22	170.51
ECAPed as-cast-T6, 4 passes	0.761	40.40
Cooling slope	3.01	53.55
ECAPed cooling slope-T6, 4 passes	0.74	29.34
ECAPed cooling slope-T6, 6 passes	0.71	23.12
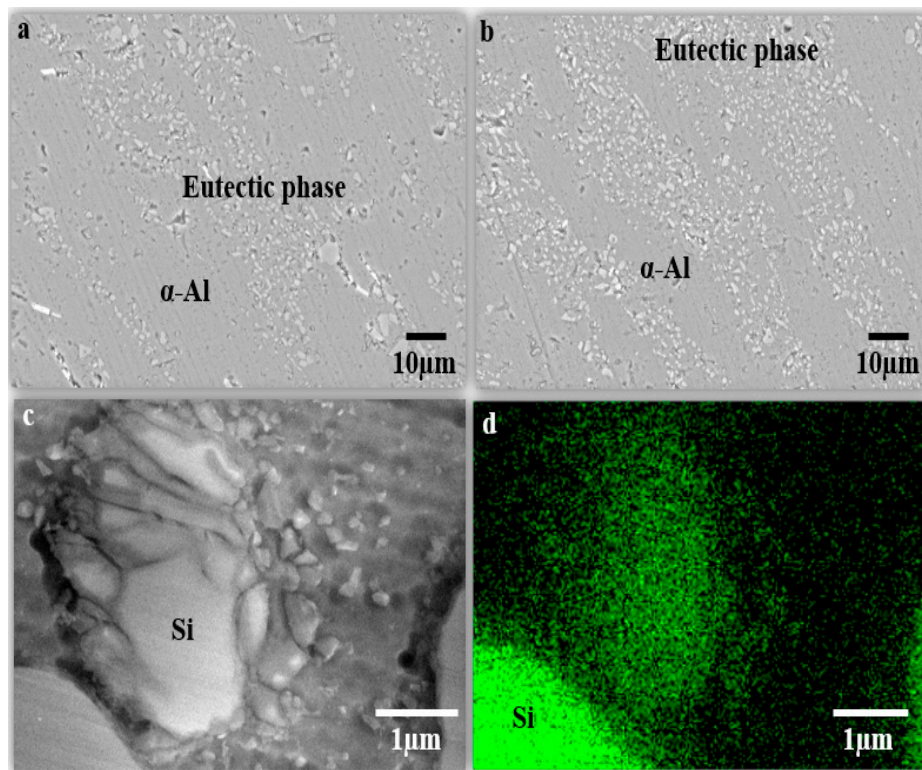
Figure 5. FESEM images: Si particles morphology after ECAP (**a**) as-cast, (**b**) cooling slope, (**c**) and (**d**) SEM and mapping of Si fragmentation of ECAPed sample.

3.5. Hardness

Figure 6a shows the Vickers microhardness of as-cast and cooling slope samples, measured after a combination of heat treatment and ECAP processing via route A. It shows that the hardness increased from 61 HV to 125 and 129 Hv, after four passes of ECAPed as-cast and cooling slope samples, respectively. After six passes, the as-cast sample failed to reach six passes, without surface cracks, while the cooling slope sample successfully reached six passes, with a 134 HV microhardness. After heat treatment, the microhardness was enhanced for the as-cast and cooling slope samples by 26% and 36%, respectively.
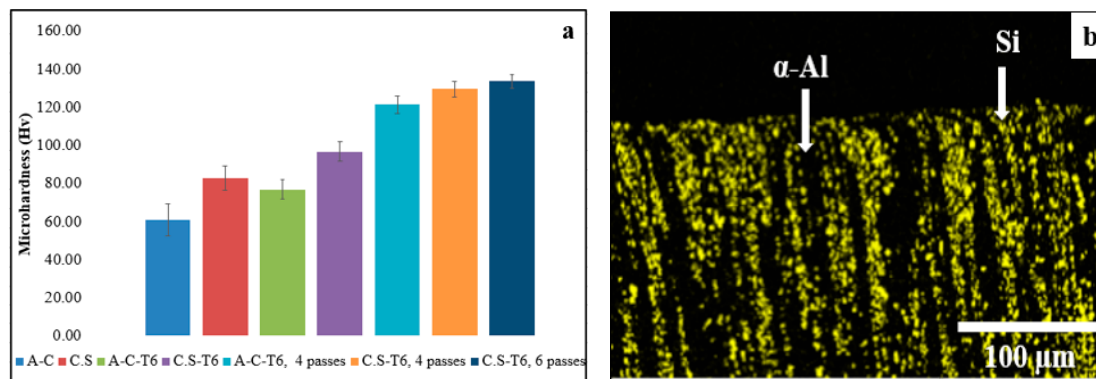
Figure 6. (**a**) Effect of T6 heat treatment and ECAP process on hardness of A356 alloy and (**b**) Mapping of silicon particles distribution in ECAPed samples.

The spheroidization of eutectic Si after T6 heat treatment was found to increase the hardness of samples. Essentially, the spheroidization of Si particles after T6 heat treatment, and the precipitation of magnesium silicide (Mg_2Si) particles during the aging process, tend to increase the ultimate tensile strength as well as hardness [47,48].

Since shear force could break down the dendrite arms of the α-Al phase, leading to grain refinement, its microstructure in the rheocasting condition became smaller and denser, where the rheocast sample recorded the highest microhardness, compared to the as-cast sample [12], as well as a change in the morphology of Si particles, from a flake shape in the as-cast to acicular shapes in the cooling slope, which contributed to the microhardness of A356 alloy, as mentioned in Section 3.2.

Four passes of ECAPed-T6 for the as-cast and cooling slope casting samples increased the hardness of both samples due to the fragmentation of globular heat-treated eutectic Si particles, the reduction in grain size, and increase in the density of dislocations. High strain, induced through six passes within the cooling slope sample during the process of ECAP, increases both the dislocation density and grain refinement as well as the fragmentation of eutectic Si particles, which led to a greater improvement in hardness, which is in line with other studies [39,49,50].

The homogenous distribution of fragmented eutectic Si particles and primary α-Al phase of the cooling slope-cast sample plays an integral role in improving the hardness of ECAPed materials. As shown in Figure 4c, the homogeneity of the distribution of the primary α-Al phase and Si particles within the eutectic mixture phase, for the microstructure of ECAPed cooling slope-cast sample, surpassed the homogeneity of a similar distribution of the ECAPed as-cast sample. Figure 6b displays the EDX map of the distribution of Si particles, after the ECAP process for the cooling slope sample. Due to the microstructural evolution, after the processes of semisolid casting, coupled with ECAP, it was expected that the finer formation and homogeneous distribution of α-Al and eutectic mixture phase enhanced the mechanical properties of the material [51].

3.6. Corrosion Resistance

3.6.1. Surface Morphology

Figure 7 reveals optical micrographs of the surface morphology, before and after the processes of ECAP, after immersion in 3.5% NaCl solution for ten days, for both the as-cast and cooling slope-cast samples. Overall, the size and the number of pitting corrosions, as well as large corrosion rings products around pits, before and after the process of ECAP, for the cooling slope-cast sample, were found to be lesser than those for the as-cast sample due to reduction and redistribution of cathodic phases after the ECAP process. Larger localized corrosion pits were found to be noticeable, for the as-cast sample. The surface morphology indicated the formation of stable pitting [52], which was attributed to a localized corrosion attack between the active particles and noble particles in a eutectic phase [53]. Essentially, the non-presence of corrosion products within the corrosion rings indicates that the cathodic

reaction occurs on rings, while the anodic reaction occurs inside the stable pit instead. Applied strain during the ECAP process reduces the grain size and develops crystalline defects, including dislocations of the grain boundary. An increase in both the area of grain boundaries and dislocations led to the formation of passive films and the corrosion of ultrafine grains, improved by the rapid formation of passive films at surface crystalline defects, including grain boundaries and dislocations [54,55]. In Al alloy, Al oxide film, containing eutectic Si particles, improved the pitting corrosion resistance by increasing the ECAP pass number, which was related to the decrease of the size of Si-containing impurities, because Si is the major cause of pitting corrosion. The decreases of the cathodic area led to a consequent decrease of the anodic current density [56].
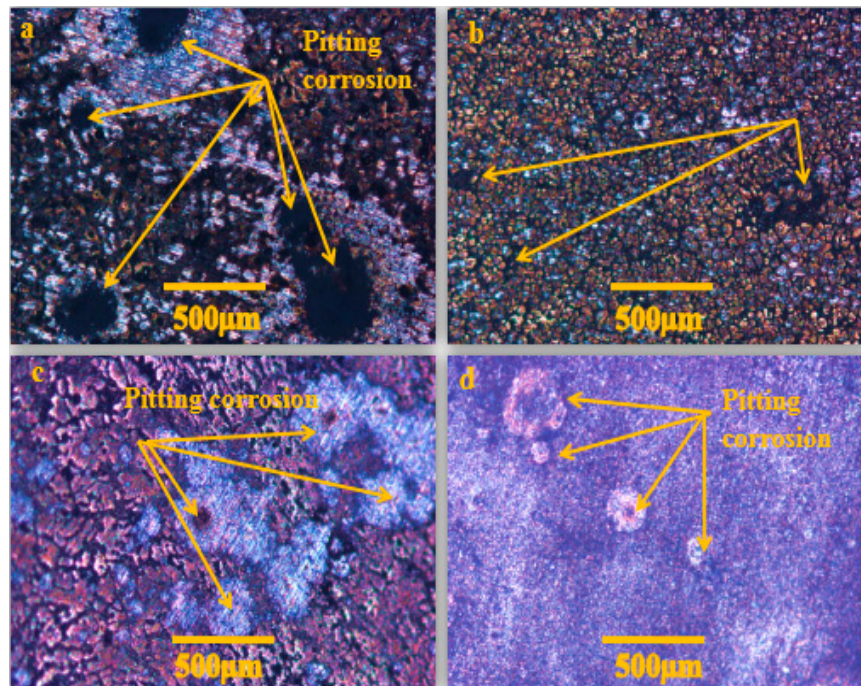
Figure 7. Surface appearance of A356 alloy (**a**) as-cast, (**b**) cooling slope (**c**) ECAPed as-cast-T6 after 4 passes and (**d**) ECAPed cooling slope-T6 after 6 passes after immersion for 10 days.

3.6.2. Potentiodynamic Test

The electrochemical behavior of A356 alloy was evaluated through the exposure of these samples to a corrosive environment, based on a simulation of sea water, using 3.5% NaCl electrolyte solution at room temperature [57]. The rate of corrosion was measured using the linear polarization technique through the Tafel extrapolation method to identify the corrosion resistance of both as-cast and cooling slope-cast samples. To compare these samples, Figure 8a–c depicts the polarization curves for the as-cast and cooling slope-cast samples, before and after the ECAP process. The corrosion performance of A356 alloy in 3.5 wt.% NaCl solution are tabulated in Table 2.

Based on the curves presented, the estimated average corrosion potentials were found to be approximately similar, with trivial differences. The results further revealed that the reduction in the corrosion rate and increment of polarization resistance, after the T6 heat treatment process for both as-cast and cooling slope-cast samples, could be attributed to the modification in the shape of certain Si particles, where these particles became substantially finer after the processes of ECAP and cooling slope casting [40]. Therefore, this could be associated with a reduction in the area ratio of cathodic to anodic phases. The corrosion rate of the as-cast alloy was 0.042 mmpy, reduced to 0.0015 mmpy after T6-4 passes route of A. Additionally, the corrosion rate of the cooling slope casting alloy was 0.019 mmpy, reduced to 0.0014 and 0.00125 mmpy after 4 and 6 passes, respectively.
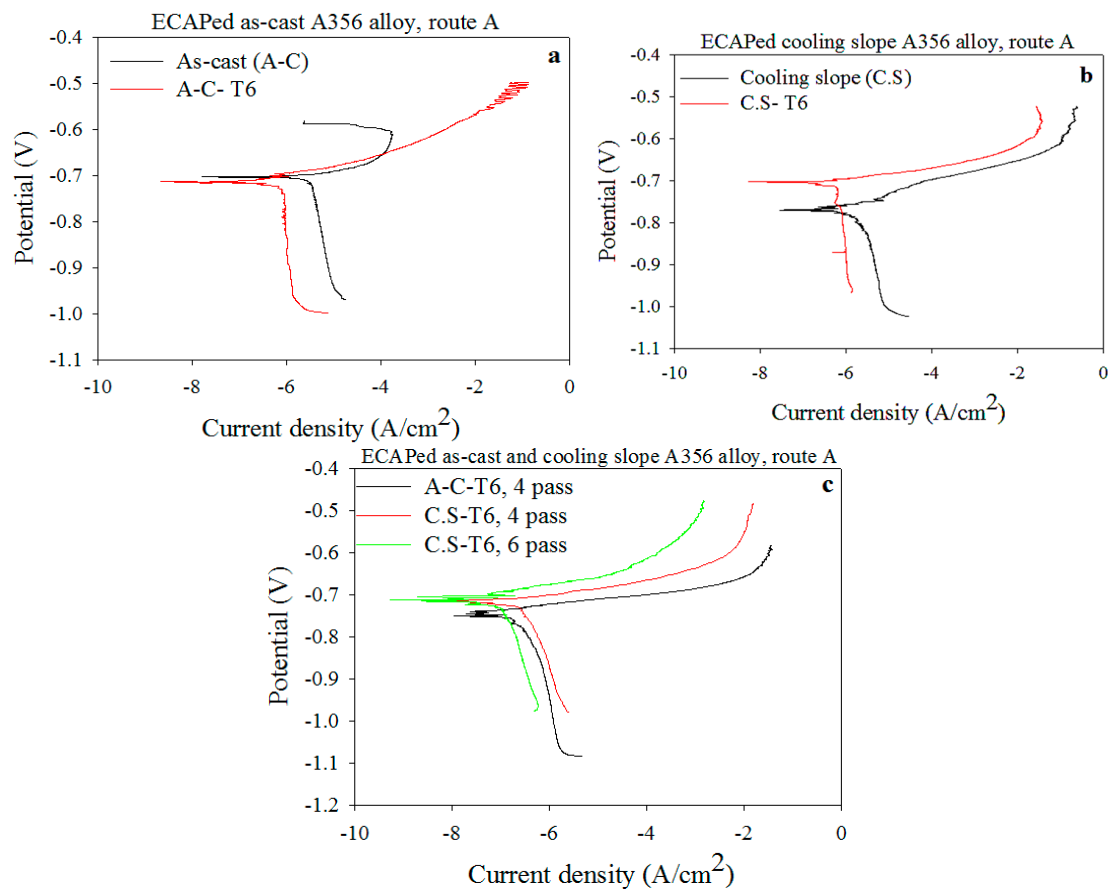
Figure 8. Polarization curves of A356 alloy before and after ECAP in 3.5 wt.% NaCl. (**a**) as-cast before and after T6; (**b**) cooling slope before and after T6; (**c**) heat-treated T6, as-cast and cooling slope after 4 and 6 passes.

Essentially, the polarization resistance depends on the microstructural state. After the ECAP process, the polarization resistance for both samples increased with more ECAP passes. Nevertheless, after the ECAP process, the polarization resistance for the as-cast sample was found to be inferior to that of cooling slope-cast sample, which positively affected the reconstruction of the metal protective layer, as shown in Table 2. However, the rate of corrosion for the heat-treated as-cast and cooling slope-cast samples decreased with more ECAP passes.

The cooling slope-cast sample mainly demonstrated an exceptional corrosion resistance, which was greater than that of the as-cast sample. The fine-grained structure, with higher grain boundaries, reduces the concentration of chloride per grain boundary, which reduces the current density [58,59], and this provides the advantage of forming more a stable and intact passivation film, improving the corrosion resistance. The obtained result in this study is in line with [60–62].

Table 2. Average of corrosion rate (CR), polarization resistance (*Rp*) and current density (*I*corr).

Samples	E_{corr} (V)	I_{corr} (A/cm^2)	Rp ($\Omega \cdot m^2$)	β_c (V·dec^{-1})	β_a (V·dec^{-1})	CR (mmy^{-1})
As-cast (A-C)	−0.698	3.894×10^{-6}	5.212×10^3	0.642	0.0504	0.0424
A-C-T6	−0.713	8.432×10^{-7}	2.035×10^4	0.443	0.0499	0.0160
A-C-T6, 4 passes	−0.751	1.369×10^{-7}	9.147×10^4	0.268	0.0286	0.0015
Cooling slope (C.S)	−0.769	1.790×10^{-6}	9.690×10^3	0.333	0.0480	0.0195
C.S-T6	−0.702	7.258×10^{-7}	2.180×10^4	0.321	0.0474	0.0079
C.S-T6, 4 passes	−0.717	1.285×10^{-7}	8.516×10^4	0.280	0.047	0.0014
C.S-T6, 6 passes	−0.709	1.145×10^{-7}	9.525×10^4	0.259	0.0466	0.00124

3.6.3. Pitting Corrosion Appearance

In the eutectic mixture phase, the initial corrosion stages of the as-cast sample revealed localized corrosion, whereas the silicon particles and α-Al interfaces were unaffected [8,32,33,49]. Figure 9 reveals a side view of the pitting corrosion of A356 alloy. Figure 9a,b displays the pitting corrosion of (a) the as-cast and (b) cooling slope-cast of A356 alloy samples. It should be noted that the presence of the enlarged area in the eutectic mixture phase in Figure 9a,b would eventually lead to a wider area of corrosion on the surface of alloy.

This implied that the microgalvanic corrosion between impurities of high Si and Al matrix could contribute to the occurrence of pitting corrosion within the area that contains impurities of high Si. Meanwhile, Figure 9c,d displays the pitting corrosion, after a potentiodynamic test for the heat-treated (c) as-cast sample (after four passes of ECAP process) and (d) cooling slope-cast sample (after six passes of ECAP process). The difference in the area of the α-Al separated grains and depth of corrosion in the eutectic mixture phase, between both the as-cast and cooling slope-cast samples, before and after the ECAP process, was evident, as revealed in Figure 9a,b. The reduction in the size of Si particles, as previously shown in Figure 5 and Table 1, the refined grain in an elongated shape, as well as the microstructure homogeneity of eutectic mixture phase surrounding the elongated α-Al phase led to the reduced rate of corrosion for the ECAPed A356-T6 cooling slope-cast alloy sample, compared to that of the as-cast alloy sample, as displayed in Figure 9c,d.
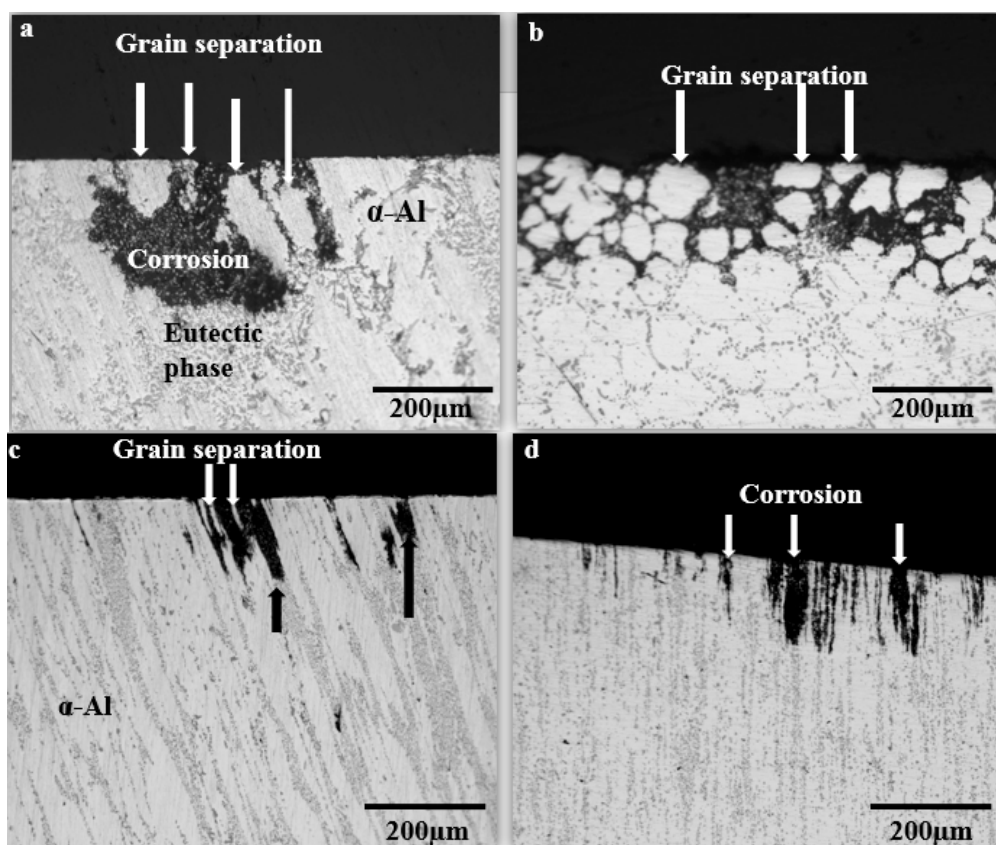
Figure 9. Pitting corrosion of (**a**) as-cast, (**b**) cooling slope, (**c**) as-cast-T6,4 passes and (**d**) cooling slope-T6, 6 passes route A of A356 alloy.

In summary, the corrosion resistance of ECAPed A356-T6 alloy sample was significantly improved due to the reduction in the galvanic potential difference, which the reduced area ratio of the noble phase to less-noble eutectic mixture phase contributed to.

The shape of Si particles influences the formation of a firm oxide film. In particular, coarsened Si particles impede the development of a protective oxide layer in the aqueous solutions and weakens the protective passive film [8]. The reduction in the area ratio of noble Si particles to less-noble eutectic Al phase around these Si particles significantly improves the resistance of pitting corrosion [5]. Furthermore, localized mechanical damage or the chemical changes of the environment may damage the protective oxide film. The increase of the applied voltage on the side of the cathodic curve, as shown in Figure 8, contributes to the rapid reduction of current to the extent that its value remains unchanged before achieving the value of I_{corr}.

The steep increment in the anodic current, with the increment in the applied potential in the positive direction, breaks the developed oxide layer and causes pitting corrosion. Here, the chloride ion attacks and dissolves the aluminum surface to form an aluminum chloride compound. The SEM image and EDX of the Al_2O_3 oxide layer of the ECAPed A356 alloy after the corrosion test, are shown in Figure 10. The highest corrosion resistance with the lowest corrosion rate were obtained for the aluminum A356 alloy, which was subjected to the ECAP process, as tabulated in Table 2.
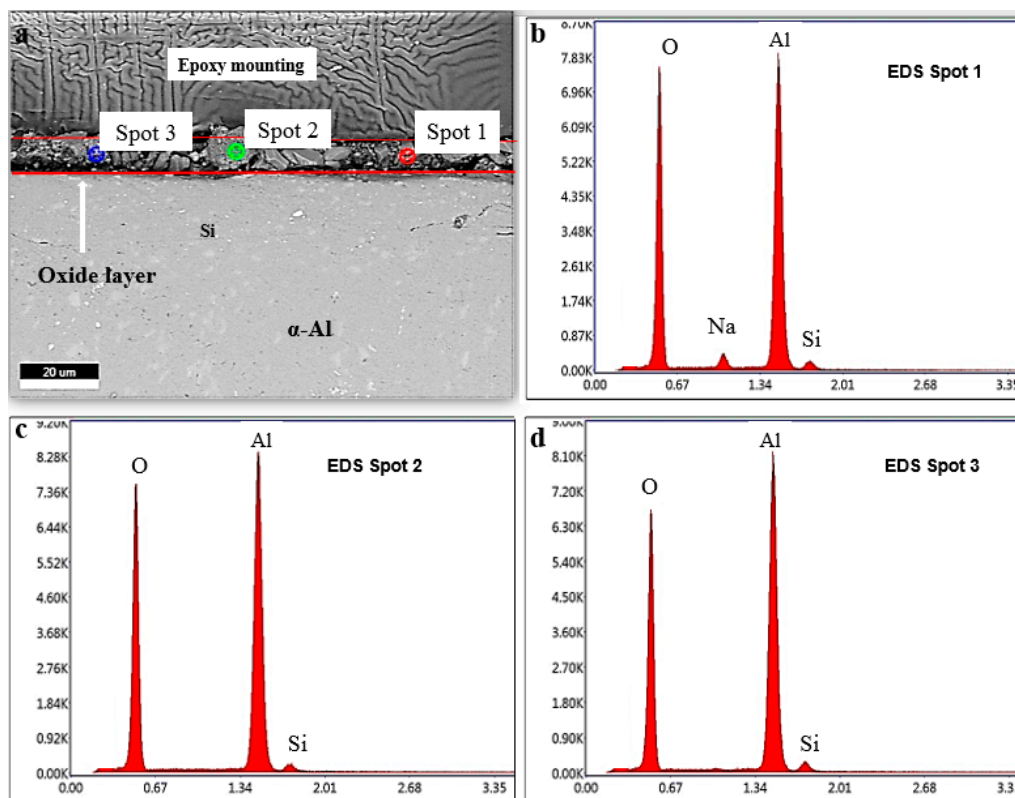
Figure 10. (**a**) Oxide layer of ECAPed A356 alloy and (**b**–**d**) EDX of oxide layer.

4. Conclusions

In this study, the microstructural evaluation of A356 alloy using heat treatment and cooling slope followed by ECAP process was successfully carried out. The effect of grain refinement on the hardness and the corrosion resistance was investigated and the results obtained can be summarized as follows:

- The as-cast samples were successfully subjected to ECAP for up to four passes, while the samples from cooling slope casting, six passes.
- The latter also showed finer and more homogeneous distribution of α-Al grains and Si particles. As a result, their hardness values were also higher.
- The combination of cooling slope casting and ECAP had given the lowest current density to the A356 alloy, at 1.145×10^{-7} A/cm^2 when experimental using 3.5 wt.% NaCl solution. The favorable

corrosion resistance was attributed to the refined Si particles that impeded the occurrences of microgalvanic cells on the protective layer of the alloy surface.

References

1. Haghdadi, N.; Zarei-Hanzaki, A.; Abedi, H.R.; Sabokpa, O. The effect of thermomechanical parameters on the eutectic silicon characteristics in a non-modified cast A356 aluminum alloy. *Mater. Sci. Eng. A* **2012**, *549*, 93–99. [CrossRef]
2. Davis, J.R. Aluminum and Aluminum Alloys. *Light Met. Alloy* **2001**, *66*, 351–416. [CrossRef]
3. Musa, A.Y.; Mohamad, A.B.; Kadhum, A.A.H.; Chee, E.P. Galvanic corrosion of aluminum alloy (Al2024) and copper in 1.0 M nitric acid. *Int. J. Electrochem. Sci.* **2011**, *6*, 5052–5065.
4. Galvin, E.; O'Brien, D.; Cummins, C.; Mac Donald, B.J.; Lally, C. A strain-mediated corrosion model for bioabsorbable metallic stents. *Acta Biomater.* **2017**, *55*, 505–517. [CrossRef] [PubMed]
5. Tahamtan, S.; Fadavi Boostani, A. Evaluation of pitting corrosion of thixoformed A356 alloy using a simulation model. *Trans. Nonferrous Met. Soc. China English Ed.* **2010**, *20*, 1702–1706. [CrossRef]
6. Boostani, A.F.; Tahamtan, S. Fracture behavior of thixoformed A356 alloy produced by SIMA process. *J. Alloys Compd.* **2009**, *481*, 220–227. [CrossRef]
7. Tahamtan, S.; Boostani, A.F. Quantitative analysis of pitting corrosion behavior of thixoformed A356 alloy in chloride medium using electrochemical techniques. *Mater. Des.* **2009**, *30*, 2483–2489. [CrossRef]
8. Barbucci, A.; Bruzzone, G.; Delucchi, M.; Panizza, M.; Cerisola, G. Breakdown of passivity of aluminium alloys by intermetallic phases in neutral chloride solution. *Intermetallics* **2000**, *8*, 305–312. [CrossRef]
9. Wang, Q.G. Microstructural effects on the tensile and fracture behavior of aluminum casting alloys A356/357. *Metall. Mater. Trans. A* **2003**, *34*, 2887–2899. [CrossRef]
10. Arrabal, R.; Mingo, B.; Pardo, A.; Mohedano, M.; Matykina, E.; Rodríguez, I. Pitting corrosion of rheocast A356 aluminium alloy in 3.5 wt.% NaCl solution. *Corros. Sci.* **2013**, *73*, 342–355. [CrossRef]
11. Akhter, R.; Ivanchev, L.; Burger, H.P. Effect of pre/post T6 heat treatment on the mechanical properties of laser welded SSM cast A356 aluminium alloy. *Mater. Sci. Eng. A* **2007**, *447*, 192–196. [CrossRef]
12. Liao, B.; Park, Y.; Ding, H. Effects of rheocasting and heat treatment on microstructure and mechanical properties of A356 alloy. *Mater. Sci. Eng. A* **2011**, *528*, 986–995. [CrossRef]
13. Syarif, J.; Detak, Y.P.; Ramli, R. Modeling of Correlation between Heat Treatment and Mechanical Properties of Ti–6Al–4V Alloy Using Feed Forward Back Propagation Neural Network. *ISIJ Int.* **2010**, *50*, 1689–1694. [CrossRef]
14. Atkinson, H. Current status of semi-solid processing of metallic materials. *Adv. Mater. Form.* **2007**, 81–98. [CrossRef]
15. Mohammed, M.N.; Omar, M.Z.; Salleh, M.S.; Alhawari, K.S.; Kapranos, P. Semisolid metal processing techniques for nondendritic feedstock production. *Sci. World J.* **2013**, *2013*, 1–16. [CrossRef] [PubMed]
16. Salleh, M.S.; Omar, M.Z.; Syarif, J.; Mohammed, M.N. An Overview of Semisolid Processing of Aluminium Alloys. *ISRN Mater. Sci.* **2013**, *2013*, 1–9. [CrossRef]
17. Spencer, D.B.; Merhrabian, R.; Flemings, M. Rheological behaviour of Sn-15pct Pb in the crystallization range. *Metall. Trans.* **1972**, *3*, 1925–1932. [CrossRef]
18. Haga, T.; Kapranos, P. Billetless simple thixoforming process. *J. Mater. Process. Technol.* **2002**, *130–131*, 581–586. [CrossRef]
19. Birol, Y. A357 thixoforming feedstock produced by cooling slope casting. *J. Mater. Process. Technol.* **2007**, *186*, 94–101. [CrossRef]

20. Mohamed, I.F.; Masuda, T.; Lee, S.; Edalati, K.; Horita, Z.; Hirosawa, S.; Matsuda, K.; Terada, D.; Omar, M.Z. Strengthening of A2024 alloy by high-pressure torsion and subsequent aging. *Mater. Sci. Eng. A* **2017**, *704*, 112–118. [CrossRef]

21. Fritsch, S.; Wagner, M.F.-X. On the effect of natural aging prior to low temperature ECAP of a high-strength aluminum alloy. *Metals* **2018**, *8*, 63. [CrossRef]

22. Wei, J.; Huang, G.; Yin, D.; Li, K.; Wang, Q.; Zhou, H. Effects of ECAP and Annealing Treatment on the Microstructure and Mechanical Properties of Mg-1Y (wt.%) Binary Alloy. *Metals* **2017**, *7*, 119. [CrossRef]

23. Shin, D.H.; Kim, B.C.; Park, K.T.; Choo, W.Y. Microstructural changes in equal channel angular pressed low carbon steel by static annealing. *Acta Mater.* **2000**, *48*, 3245–3252. [CrossRef]

24. Abd El Aal, M.I.; Sadawy, M.M. Influence of ECAP as grain refinement technique on microstructure evolution, mechanical properties and corrosion behavior of pure aluminum. *Trans. Nonferr. Met. Soc. China Engl. Ed.* **2015**, *25*, 3865–3876. [CrossRef]

25. Moradi, M.; Nili-Ahmadabadi, M.; Heidarian, B. Improvement of mechanical properties of AL (A356) cast alloy processed by ecap with different heat treatments. *Int. J. Mater. Form.* **2009**, *2*, 85–88. [CrossRef]

26. Jiang, J.-H.; Ma, A.-B.; Lu, F.-M.; Saito, N.; Watazu, A.; Song, D.; Zhang, P.; Nishida, Y. Improving corrosion resistance of Al-11mass% Si alloy through a large number of ECAP passes. *Mater. Corros.* **2011**, *62*, 848–852. [CrossRef]

27. Jiang, J.; Ma, A.; Song, D.; Yang, D.; Shi, J.; Wang, K.; Zhang, L.; Chen, J. Anticorrosion behavior of ultrafine-grained Al-26 wt% Si alloy fabricated by ECAP. *J. Mater. Sci.* **2012**, *47*, 7744–7750. [CrossRef]

28. Wang, X.; Nie, M.; Wang, C.T.; Wang, S.C.; Gao, N. Microhardness and corrosion properties of hypoeutectic Al-7Si alloy processed by high-pressure torsion. *Mater. Des.* **2015**, *83*, 193–202. [CrossRef]

29. Osório, W.R.; Garcia, L.R.; Goulart, P.R.; Garcia, A. Effects of eutectic modification and T4 heat treatment on mechanical properties and corrosion resistance of an Al-9 wt% Si casting alloy. *Mater. Chem. Phys.* **2007**, *106*, 343–349. [CrossRef]

30. Tahamtan, S.; Fadavi Boostani, A. Microstructural characteristics of thixoforged A356 alloy in mushy state. *Trans. Nonferr. Met. Soc. China Engl. Ed.* **2010**, *20*, s781–s787. [CrossRef]

31. Samsudin, M.; Omar, M.Z.; Abdullah, S. Effects of rheocasting and thixoforming on the microstructure and mechanical properties of A356 aluminium alloy. *J. Teknol.* **2016**, *78*, 107–113.

32. Rooy, E.L.; Linden, J.H.L. *Van ASM Metals Handbook, Vol 02 Properties and Selection: Nonferrous Alloys and Special-Purpose Materials*; ASM International: Geauga, OH, USA, 1990; pp. 3330–3345.

33. Kurz, W.; Fisher, D. *Fundamentals of Solidification*; Trans Tech Publication Ltd.: Aedermannsdorf, Switzerland, 1986; ISBN 0878495223.

34. Flemings, M.C. Behavior of metal alloys in the semisolid state. *Metall. Trans. B* **1991**, *22*, 269–293. [CrossRef]

35. Ogris, E.; Wahlen, A.; Lüchinger, H.; Uggowitzer, P.J. On the silicon spheroidization in Al-Si alloys. *J. Light Met.* **2002**, *2*, 263–269. [CrossRef]

36. Tiryakioğlu, M. Si particle size and aspect ratio distributions in an Al-7%Si-0.6%Mg alloy during solution treatment. *Mater. Sci. Eng. A* **2008**, *473*, 1–6. [CrossRef]

37. Li, B.; Wang, H.; Jie, J.; Wei, Z. Effects of yttrium and heat treatment on the microstructure and tensile properties of Al-7.5Si-0.5Mg alloy. *Mater. Des.* **2011**, *32*, 1617–1622. [CrossRef]

38. Ishak, N.N.M.; Salleh, M.S.; Yahaya, S.H.; Mohamad, E.; Sulaiman, M.A. The Effect of Equal Channel Angular Pressing (ECAP) on the Microstructure and Hardness of A356 Aluminium Alloy. *J. Adv. Manuf. Technol.* **2017**, *11*, 47–58.

39. Cepeda-Jiménez, C.M.; García-Infanta, J.M.; Zhilyaev, A.P.; Ruano, O.A.; Carreño, F. Influence of the supersaturated silicon solid solution concentration on the effectiveness of severe plastic deformation processing in Al–7 wt.% Si casting alloy. *Mater. Sci. Eng. A* **2011**, *528*, 7938–7947. [CrossRef]

40. Ritwik, R.; Rao, A.K.P.; Dhindaw, B.K. Low-convection-cooling slope cast AlSi7Mg alloy: A rheological perspective. *J. Mater. Eng. Perform.* **2013**, *22*, 2487–2492. [CrossRef]

41. Natori, K.; Utsunomiya, H.; Tanaka, T. Improvement in formability of semi-solid cast hypoeutectic Al-Si alloys by equal-channel angular pressing. *J. Mater. Process. Technol.* **2017**, *240*, 240–248. [CrossRef]

42. Mill, E.B.; Sherif, E.M.; Mohammed, J.A.; Abdo, H.S.; Almajid, A.A. Corrosion Behavior in Highly Concentrated Sodium Chloride Solutions of Nanocrystalline Aluminum Processed by High. *Int. J. Electrochem. Sci.* **2016**, *11*, 1355–1369.

43. Nguyen, V.T.; Hussain, Z.; Anasyida, A.S.; Huy, T.D.; Almanar, I.P. Influence of Semi-Solid Casting and Equal Channel Pressing on Microstructure of a Hypoeutectic Al-Si Alloy. *Mater. Sci. Forum* **2015**, *819*, 9–14. [CrossRef]

44. Rollett, A.; Humphreys, F.; Rohrer, G.; Hatherly, M. *Recrystallization and Related Annealing Phenomena*; Elsevier Science Ltd.: Oxford, UK, 2004.

45. Mckenzie, P.W.J.; Lapovok, R.; Estrin, Y. The influence of back pressure on ECAP processed AA 6016: Modeling and experiment. *Acta Mater.* **2007**, *55*, 2985–2993. [CrossRef]

46. Meyers, M.A.; Mishra, A.; Benson, D.J. Mechanical properties of nanocrystalline materials. *Prog. Mater. Sci.* **2006**, *51*, 427–556. [CrossRef]

47. Zhu, M. Effects of T6 heat treatment on the microstructure, tensile properties, and fracture behavior of the modified A356 alloys. *J. Mater.* **2017**, *36*, 243–249. [CrossRef]

48. Möller, H.; Govender, G.; Stumpf, W. Factors influencing tensile mechanical properties of Al-7Si-Mg casting alloys A356/7. In *Light Alloys 2012*; Springer: Berlin, Germany, 2012; pp. 467–471.

49. Goodarzy, M.H.; Arabi, H.; Boutorabi, M.A.; Seyedein, S.H.; Najafabadi, S.H.H. The effects of room temperature ECAP and subsequent aging on mechanical properties of 2024 Al alloy. *J. Alloys Compd.* **2014**, *585*, 753–759. [CrossRef]

50. Kumar, S.R.; Gudimetla, K.; Venkatachalam, P.; Ravisankar, B.; Jayasankar, K. Microstructural and mechanical properties of Al 7075 alloy processed by Equal Channel Angular Pressing. *Mater. Sci. Eng. A* **2012**, *533*, 50–54. [CrossRef]

51. Thuong, N.; Zuhailawati, H.; Seman, A.A.; Huy, T.D.; Dhindaw, B.K. Microstructural evolution and wear characteristics of equal channel angular pressing processed semi-solid-cast hypoeutectic aluminum alloys. *Mater. Des.* **2015**, *67*, 448–456. [CrossRef]

52. Hughes, A.E.; Birbilis, N.; Mol, J.M.C.; Garcia, S.J.; Zhou, X.; Thompson, G.E. Corrosion and principles of protection. In *Recent Trends in Processing and Degradation of Aluminium Alloys*; Intech: Rijeka, Croatia, 1968.

53. Birbilis, N.; Buchheit, R.G. Electrochemical Characteristics of Intermetallic Phases in Aluminum Alloys: An Experimental Survey and Discussion. *J. Electrochem. Soc.* **2005**, *152*, 140–151. [CrossRef]

54. Boag, A.; Hughes, A.E.; Glenn, A.M.; Muster, T.H.; McCulloch, D. Corrosion of AA2024-T3 Part I: Localised corrosion of isolated IM particles. *Corros. Sci.* **2011**, *53*, 17–26. [CrossRef]

55. Balyanov, A.; Kutnyakova, J.; Amirkhanova, N.A.; Stolyarov, V.V.; Valiev, R.Z.; Liao, X.Z.; Zhao, Y.H.; Jiang, Y.B.; Xu, H.F.; Lowe, T.C.; et al. Corrosion resistance of ultra fine-grained Ti. *Scr. Mater.* **2004**, *51*, 225–229. [CrossRef]

56. Di Schino, A.; Kenny, J.M. Effects of the grain size on the corrosion behavior of refined AISI 304 austenitic stainless steels. *J. Mater. Sci. Lett.* **2002**, *21*, 1631–1634. [CrossRef]

57. Yahya, S.; Rahim, A.A. Inhibitive Behaviour of Corrosion of Aluminium Alloy in NaCl by Mangrove Tannin. *Sains Malaysiana* **2011**, *40*, 953–957.

58. Inturi, R.B. Localized Corrosion of Nanocrystalline 304 Type Stainless Steel Films. *Corrosion* **1992**, *48*, 398–403. [CrossRef]

59. Rashida, S.; Islamia, N.; Ariffina, A.K.; Ridhab, M.; Fonnab, S. The effect of immersion time on the corrosion behavior of SUS304 in brine using half-cell potential measurement. *Polarization* **2016**, *5*, 7.

60. Krishna, K.G.; Sivaprasad, K.; Narayanan, T.S.N.S.; Kumar, K.C.H. Localized corrosion of an ultrafine grained Al–4Zn–2Mg alloy produced by cryorolling. *Corros. Sci.* **2012**, *60*, 82–89. [CrossRef]

61. Akiyama, E.; Zhang, Z.; Watanabe, Y. Effects of severe plastic deformation on the corrosion behavior of aluminum alloys. *J. Solid State Electrochem.* **2009**, *13*, 277–282. [CrossRef]

62. Song, D.; Ma, A.; Jiang, J.; Lin, P.; Yang, D. Corrosion behavior of ultra-fine grained industrial pure Al fabricated by ECAP. *Trans. Nonferr. Met. Soc. China Engl. Ed.* **2009**, *19*, 1065–1070. [CrossRef]